Biosensors and Bioelectronics 208 (2022) 114216

Contents lists available at ScienceDirect

Biosensors and Bioelectronics

journal homepage: www.elsevier.com/locate/bios

Magnetic antifouling material based ratiometric electrochemical biosensor for the accurate detection of CEA in clinical serum

Huiqing Yang, Yan Xu, Qianqian Hou, Qingzhang Xu, Caifeng Ding *

Key Laboratory of Optic-electric Sensing and Analytical Chemistry for Life Science, Ministry of Education, Shandong Key Laboratory of Biochemical Analysis, Key Laboratory of Analytical Chemistry for Life Science in Universities of Shandong, College of Chemistry and Molecular Engineering, Qingdao University of Science and Technology, Qingdao, 266042, PR China

ARTICLE INFO

Keywords:
Electrochemical biosensor
Ratiometric strategy
MXene
Anti-fouling
Carcinoembryonic antigen

ABSTRACT

A novel ratio electrochemical biosensor based on multi-functional nanocomposite was developed. Fe_3O_4 was synthesized in situ on carboxyl functionalized 2D nanomaterial MXene, and then covalently bonded with $[Ru(NH_3)_6]^{3+}$ to obtain nanocomposites MXC-Fe_3O_4-Ru. Fe_3O_4 and $[Ru(NH_3)_6]^{3+}$ can neutralize the electronegativity of the MXene to make the nanocomposites electrically neutral. Combine with the good hydrophilicity and conductivity of MXene, the nanocomposites can be utilized to construct antifouling electrochemical biosensors without modifying with specific antifouling materials. Moreover, Fe_3O_4 can endow the nanocomposites with magnetism, and $[Ru(NH_3)_6]^{3+}$ is used as an internal standard molecule. The strong magnetic MXC-Fe_3O_4-Ru can be easily separated and firmly modified on the magnetic gold electrode (MGE). DNA double-stranded (dsDNA) containing an ferrocene (Fc)-modified carcinoembryonic antigen (CEA) aptamer can be specifically captured to the surface of the electrode by amido bond. In the presence of CEA, CEA binds to the aptamer and leaves the electrode surface, the electrochemical signal of Fc decreases, while the electrochemical signal of $[Ru(NH_3)_6]^{3+}$ is fixed on the electrode surface remains basically unchanged. The ratio of the electrochemical signals of Fc and $[Ru(NH_3)_6]^{3+}$ is proportional to the CEA concentration. The linear range of the sensor is 1 pg/mL to 1 μg/mL with a detection limit of 0.62 pg/mL. With the excellent antifouling performance, good conductivity of the nanocomposite, and the application of the ratiometric strategy, the biosensor can achieve high selectivity, accuracy, and sensitivity for the detection of targets even in complex samples, such as FBS and clinical serum.

1. Introduction

In recent years, cancer has become one of the main causes of death in the world, early and accurate diagnosis of this kind of malignant tumor is very important for human health. As a widely used tumor biomarker in the clinic, carcinoembryonic antigen (CEA) is highly expressed in many tumor tissues, such as pancreatic cancer (Steward et al., 1974), colorectal cancer (Miao et al., 2014), cervical cancer (Qiu et al., 2018), breast cancer (Huang et al., 2010) and cystadenocarcinoma (Tang et al., 2011). Therefore, establishing a sensitive, simple, and accurate method for CEA detection is of great significance for early diagnosis of cancer and improving the survival rate of patients.

Aptamers, which are screened in vitro based on systemic evolution of ligands by exponential enrichment, have been an alternative to antibodies with the advantages of low cost, easy synthesis, structure-switching capability, and long-term stability (Raston and Gu, 2015; Kim et al., 2019a, 2019b; Breaker, 2004). The biosensors based on aptamers have been reported by various groups in recent years. For instance, Liu's group designed an aptasensor based on resonance energy transfer and showed excellent sensing performance (Wu et al., 2015), Fan's group has applied the aptamer to the photoelectrochemical sensing platform (Lu et al., 2021). The aptamer against CEA (5′-ATA CCA GCT TAT TCA ATT-3′), which has good affinity and specificity (Wu et al., 2015; Ma et al., 2021), has been widely used for the detection of CEA since it was first reported in 2013 (Smith, 2013).

Recently, various analytical technologies have been reported to detection biomarkers, including surface enhanced Raman spectroscopy (Sun et al., 2016), chemiluminescence immunoassay (He et al., 2015), fluorescence method (Song et al., 2013), and electrochemical technology (Zhou et al., 2016). Electrochemical as an analysis technique has been widely used with the advantages of simplicity, low cost, high specificity, and sensitivity (Martín et al., 2017). However, better

* Corresponding author.
E-mail address: dingcaifeng@qust.edu.cn (C. Ding).

https://doi.org/10.1016/j.bios.2022.114216
Received 25 November 2021; Received in revised form 17 March 2022; Accepted 21 March 2022
Available online 25 March 2022

conductivity and low-fouling are still very important for the research of electrochemical sensors, which can further improve the sensitivity and selectivity of the biosensors, and achieve accurate detection in the complex environment of real samples.

Biofouling in the sensing process, which was mainly caused by the non-specific protein adsorption is a serious challenge for electrochemical analysis in complex practical applications. A series of antifouling materials with hydrophilicity and electric neutrality have been applied for the surface modification of electrochemical sensors. As the most mature commercial antifouling material, PEG has been widely used in sensors and electronic products (Hui et al., 2017; Wang et al., 2017; Luo et al., 2014; Cui et al., 2016), but serious oxidation during the usage will greatly impair the anti-fouling performance (Zhang et al., 2017). Zwitterionic materials also have the excellent antifouling ability and can form hydrated shells through ionic solvation (Liu et al., 2016), but the synthesis process is complex, which greatly limits their application. In recent years, peptides have become a suitable choice for antifouling materials because of their controllable structure, easy preparation, and environmental friendliness (Ding et al., 2019; Wang et al., 2020; Liu et al., 2018), but the poor conductivity will inevitably hinder the electron transfer on the electrode surface and affect the sensitivity of the biosensor.

To obtain a high-performing electrochemical sensing interface, 2D nanomaterials with large specific surface area, good conductivity, excellent physical and chemical properties, have gradually attracted people's attention and have been broad applicated in electrochemical biosensors (Chimene et al., 2015; Zhuang et al., 2015). Among them, early transition metal carbides, nitrides, or carbonitrides (MXene), as a recently developed 2D nanomaterial, show unique functions in bioanalytical applications, including high metal conductivity, high ion transport performance, large surface area, low diffusion barrier, easy surface functionalization, biocompatibility, good passivation resistance and pollution resistance (Naguib et al., 2014; Liu et al., 2018; Liang et al., 2015; Yan et al., 2017). The surface of MXene etched by hydrofluoric acid (HF) contains functional groups, which are easy to be functionalized on its surface (Li et al., 2018b). It is worth noting that MXene has good reduction ability, unique folding structure, and compatibility with other materials, which makes it easy to combine with other different materials, thus further improving its electrochemical sensing performance (Xu et al., 2021; Zhang et al., 2020b, 2021a).

In our previous work, we developed an antifouling electrochemical biosensor based on 2D nanomaterial MXene loaded with gold nanoparticles (AuNPs) for the detection of CEA. In that work, MXene loaded with AuNPs not only greatly improve the specific surface area and conductivity of the sensing surface, but also acted as the carrier of the internal standard molecular of methylene. To realize the antifouling performance of the biosensor, multifunctional peptides were designed and modified to the surface of AuNPs loaded on the MXene. In the present work, considering the inherent hydrophilicity and electronegativity of MXene, the Fe_3O_4 was generated in situ on the surface of the MXene and the internal standard molecule ruthenium hexamine ($[Ru(NH_3)_6]^{3+}$) was covalently introduced to the carboxyl group of Mexene to obtain the nanocomposite MXC-Fe_3O_4-Ru with high conductivity, biocompatibility, hydrophilicity, and electric neutrality because Fe_3O_4 and $[Ru(NH_3)_6]^{3+}$ have good electric neutralization effect on MXene (Yadav et al., 2020). In addition, the nanocomposite MXC-Fe_3O_4-Ru can be easily separated due to the inherent magnetism of Fe_3O_4. Thus, the nanocomposite MXC-Fe_3O_4-Ru was absorbed to the surface of the magnetic electrode to construct a ratiometric antifouling electrochemical biosensor for the detection of CEA with high accuracy, selectivity, and sensitivity, even in complex biological systems due to the antifouling performance of the nanocomposite MXC-Fe_3O_4-Ru and the self calibration of ratiometric strategy.

2. Experimental section

2.1. Synthesis of Ti_3C_2Tx-MXene

Ti_3C_2Tx-MXene was synthesized according to the reference with a slight modification (Alhabeb et al., 2017). Briefly, 2.0 mg of Ti_3AlC_2 was added to 8 mL of 40% HF solution and stirred reaction for 48 h to etch the Al in Ti_3AlC_2. The obtained product was repeatedly centrifuged and washed with deionized water until the pH of the supernatant was greater than 6. Then the precipitate was dried in vacuum.

2.2. Synthesis of carboxyl modified MXene

MXC was synthesized according to reference (Liu et al., 2018). 20 mg MXene was sonicated in 12 mL water for 30 min and then 0.17 g of $ClCH_2COOH$ was added under stirring at 0 °C for 40 min, and NaOH (640 μL, 6.25 M) was added at 60 °C. After stirring for 3 h, the product was centrifugally washed by deionized water and dried in vacuum at 60 °C to obtain MXC.

2.3. Synthesis of MXC-Fe_3O_4-Ru

MXC was dispersed in 2 mL deionized water and sonicated for 30 min to disperse evenly. Under the protection of N_2, 8.00 mM $FeSO_4{\cdot}7H_2O$ and 16.0 mM $FeCl_3{\cdot}6H_2O$ were added under stirring at 80 °C, and 30% ammonia was added quickly to precipitate Fe^{2+}/Fe^{3+}. After raising the temperature to 85 °C, the pH of the mixture was adjusted to about 10 with ammonia and further reacted for 45 min. The product of MXC-Fe_3O_4 was washed by magnetic separation and redispersed into 2 mL of deionized water.

100 μL MXC-Fe_3O_4 dispersion was diluted to 500 μL in PBS containing NHS (0.100 M) and EDC (0.400 M) for 2 h to activate the carboxyl group, and then $[Ru(NH_3)_6]^{3+}$(50 μL, 1.00 mM) was added. After reaction for 2 h, the mixture was purified by magnetic separation to obtain MXC-Fe_3O_4-Ru.

2.4. Preparation of the sensing surface

Magnetic gold electrode (MGE) was first polished with Al_2O_3 powder and then cleaned with an ultrasonic bath three times, 5 μL MXC-Fe_3O_4-Ru was fixed on the electrode surface by strong magnetic force and dried at room temperature. The electrode modified with MXC-Fe_3O_4-Ru was incubated in 50 μL capture DNA solution (S1-NH_2) for 2 h to connect S1 to the electrode surface by an amide bond. At last, the modification electrode was incubated in 50.0 μM DNA2 tagged with Fc (S2-Fc) to hybridize for 2 h to construct the sensing interface.

2.5. Electrochemical measurements

The fully constructed electrode surface was incubated in CEA solutions of different concentrations for 60 min, and the electrochemical response was recorded by DPV with a scanning range of −0.5 V–0.5 V. The potential increment is 0.004 V, the pulse period is 0.5 s, and the amplitude is 0.05 V.

3. Results and discussion

3.1. Principle of the antifouling electrochemical biosensor

As can be seen from Scheme 1, a novel antifouling electrochemical biosensor was developed based on the functionalized nanomaterials MXene. The Al in Ti_3AlC_2 was selectively etched by HF to obtain accordion-like MXene with high conductivity and hydrophilicity, and further carboxyl modification in an alkaline environment to obtain functional MXC. Magnetic Fe_3O_4 was grown on MXC in situ and $[Ru(NH_3)_6]^{3+}$ was connected to MXC as an internal standard molecule by an

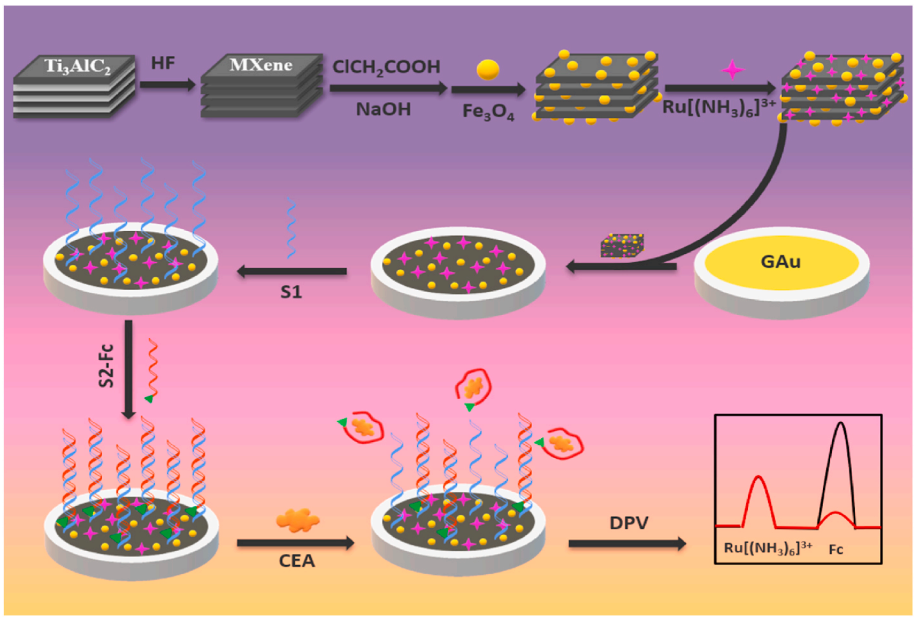

Scheme 1. Working principle diagram of the antifouling ratiometric electrochemical biosensor based on MXC-Fe_3O_4-Ru.

amide bond to obtain a new nanocomposite MXC-Fe_3O_4-Ru. Fe_3O_4 endows the magnetism and further improves the conductivity of the nanocomposite. More important, Fe_3O_4 and $[Ru(NH_3)_6]^{3+}$ can neutralize the negative charge of the MXC to obtain the electroneutral material. The strong magnetic MXC-Fe_3O_4-Ru can be easily separated and firmly modified on MGE to perform an antifouling surface. Then, MXC-Fe_3O_4-Ru on the surface of MGE was modified with S1 by covalent bond and hybridized with the Fc modified CEA aptamer to form the double-strand structure. When CEA exists, the electrochemical signal of Fc decreased because the aptamer was competed and departed away from the electrode surface, whereas the signal of $[Ru(NH_3)_6]^{3+}$ remained unchanging. The accuracy of the present biosensor achieved great improvement because the ratiometric strategy can effectively reduce the impact of instrument or environment, and eliminate the interference of the detection system through self-calibration of the two signals. More importantly, MXC-Fe_3O_4-Ru shows excellent resistance to nonspecific adsorption of proteins due to its hydrophilicity and electric neutrality without specially integration or addition of other antifouling materials, which greatly simplifies the electrode construction process, ensures the electron transfer efficiency of the electrode surface, and realizes the high selectivity detection of targets in complex samples.

3.2. *Characterization of Ti_3AlC_2, MXene, and MXC-Fe_3O_4*

The appearance of material are recorded by SEM as shown in Fig. 1. Al in Ti_3AlC_2 with a dense stacking structure (Fig. 1A) was selectively etched by HF and becomes MXene with a layered structure (Fig. 1B). As shown in Fig. 1C, magnetic Fe_3O_4 is grown in situ on the surface (or in

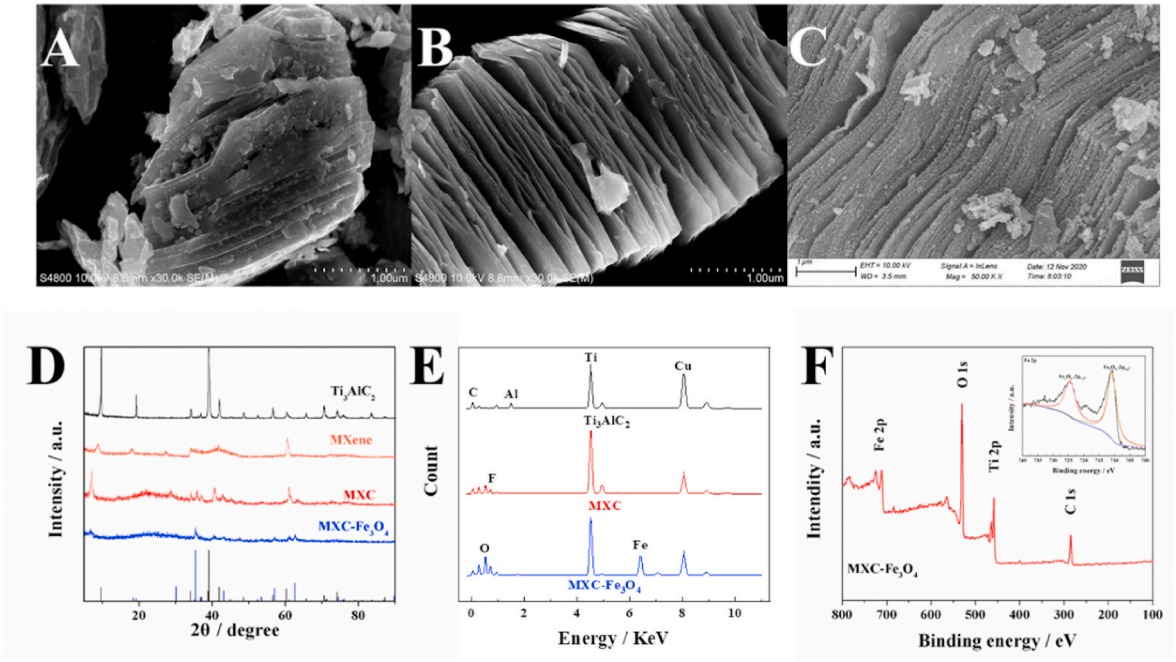

Fig. 1. SEM images of (A) Ti_3AlC_2, (B) MXene, and (C) MXC-Fe_3O_4; XRD spectra (D) and EDS spectra (E) of different materials; (F) XPS spectra of MXC-Fe_3O_4.

the fold) of MXC. Fig. 1D shows the XRD patterns of different materials, the diffraction peak of Ti_3AlC_2 corresponds to the standard card, the characteristic peaks of 9.52°, 19.15°, and 39° respectively correspond to (002), (004), and (104) facets of Ti_3AlC_2(Ding et al., 2018). After HF etching, the peak at (104) disappeared, indicating the disappearance of Al, and the peaks at (002) and (004) moved to 8.5° and 18.04°, indicating that the d-spacing increased, which is in good agreement with SEM images. After carboxyl modification, the peak at (002) moved to 6.76 and the peak at (004) disappeared, which indicates that the carboxyl group was modified in MXene (Li et al., 2018a). After in-situ synthesis of Fe_3O_4, the characteristic diffraction peaks at 35.45°, 43.09°, 56.98°, and 62.57° appeared respectively, which also corresponds well with the standard card of Fe_3O_4. From Fig. 1E, we can see that the Al element disappeared and the F element appeared, the O element appeared and the proportion of the C element increased, and all these results ascribed to the HF etching and the modification of the carboxyl group. Fig. 1F shows the XPS analysis of MXC-Fe_3O_4. Through the peak splitting of Fe2p, it is proved that Fe_3O_4 nanoparticles are indeed synthesized in situ. It can be seen from the above characterization that the material has been successfully prepared as expected.

3.3. Electrochemical behavior of nanocomposites

The specific surface areas of bare MGE, MXC/MGE, and MXC-Fe_3O_4/MGE were measured according to the electrochemical method, as shown in Fig. S1. According to Randles-Sevcik equation: $Ip = 2.69 \times 10^5 AD^{1/2}cv^{1/2}$. Here, Ip is the peak current (in A), A is the electrochemical active area (in cm^2), D is the diffusion coefficient of 5 mM $[Ru(NH_3)_6]^{3+}$ (6.0×10^{-6} cm^2/s), c is the concentration of $[Fe(CN)_6]^{3-/4-}$ (5×10^{-3} M), and v is the scan rate (in V/s). The CV curves of electrode surfaces with different modified materials in 5 mM $[Ru(NH_3)_6]^{3+}$ at different scanning speeds were measured, and their electrochemical active areas were calculated. After calculated by equation, the specific surface area of bare MGE, MXC/MGE, and MXC-Fe_3O_4/MGE is 0.08291 cm^2, 0.16230 cm^2, and 0.26577 cm^2, respectively. The electrochemical active area increased significantly after modification, and thus the performance of the sensor can be enhanced greatly.

3.4. Generic antifouling characteristics

The hydrophilicity of the constructed electrode surface was evaluated by the static water contact angle. As shown in Fig. S2 and Table S1, compared with bare MGE, the static water contact angle of MXC-Fe_3O_4-Ru/MGE is reduced from 71.66° to 23.42°, which is ascribed to the large number of hydrophilic groups on MXC. After dsDNA was captured, the static water contact angle increased slightly to 29.01° due to the hydrophobicity of the DNA. But the whole electrochemical sensor interface still shows favorable hydrophilicity because the Fc labeled on the DNA is slightly soluble in water.

Zeta potential tests were carried out for materials at different stages, as shown in Fig. S3. MXene is negatively charged (Fig. S3A) and Fe_3O_4 is positively charged (Fig. S3B). After carboxyl functionalization, the zeta potential of MXC becomes further negative (Fig. S3C). After modifying Fe_3O_4, Fe_3O_4 has a very obvious electrical neutralization to MXC (Fig. S3D). Subsequently, after $[Ru(NH_3)_6]^{3+}$ is covalently connected to MXC-Fe_3O_4, the zeta potential tends to be electrically neutral (Fig. S3E).

To testify the antifouling performance of the constructed electrode, the electrode before and after modification were immersed in different concentrations FBS, incubated for 30 min, and the electrochemical signal changes were recorded as shown in Fig. 2A and B. From Fig. 2C we can see that the DPV signal of bare MGE decreased by 19.89% after incubation in FBS, while the signal of Fc on the antifouling interface decreased by only 6.05%. The result shows that constructed sensor interface has good antifouling performance and can resist most of the

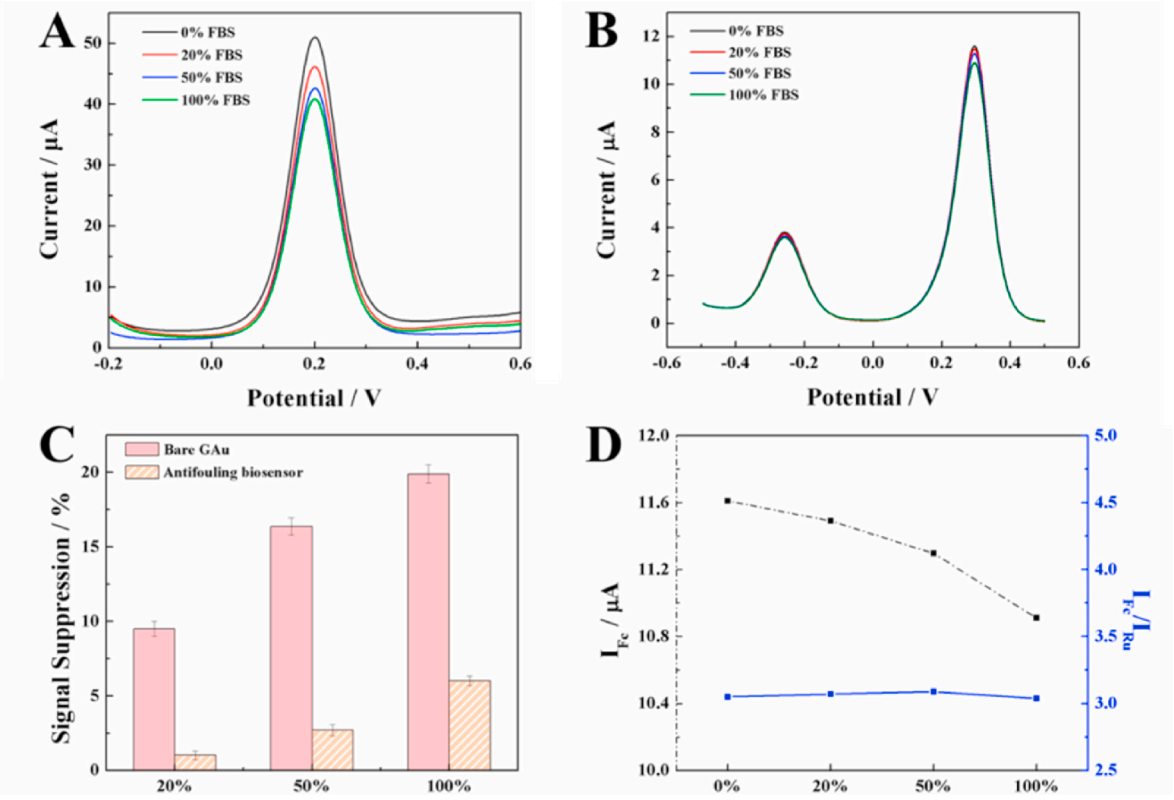

Fig. 2. (A) DPV response of bare MGE in 5 mM $[Fe(CN)_6]^{3-/4-}$ before and after incubation in different concentrations of FBS; (B) DPV response of biosensor in PBS before and after incubation FBS with different concentrations; (C) Comparison of antifouling performance of different electrode surfaces; (D) The antifouling performance correction of the ratio signal to the single signal.

non-specific adsorption because the protein and other impurities adsorbed on the electrode surface will seriously hinder the transmission of electrons.

In addition, the signal change of the biosensor constructed with and without molecules in the antifouling evaluation process are analyzed. As shown in Fig. 2D, when there is no internal standard molecules, the DPV signal of Fc has an obvious downward trend with the increase of FBS concentration. When there were internal standard molecules, the ratio signal of probe Fc to an internal standard molecule of $[Ru(NH_3)_6]^{3+}$ almost unchanged, which shows the introduction of internal standard molecules can effectively avoid the interference caused by the environment and improve the accuracy of detection.

3.5. Feasibility and construction of the biosensing

The feasibility and surface construction of the sensor were characterized by gel electrophoresis, DPV, and CV. The feasibility of DNA chain hybridization was proved by gel electrophoresis analysis was shown in Fig. S4, the S1-NH_2 and CEA aptamer strand S2-FC correspond to lane 1 and lane 2, a significantly higher band representing the hybridization of the S1-NH_2 and S2-FC were observed in lane 3, and this is due to the larger molecular weight of dsDNA. From Fig. 3A, we can see that the DPV curve of bare MGE (curve a) have no peak, after MXC-Fe_3O_4-Ru was modified on the surface, the DPV signal of $[Ru(NH_3)_6]^{3+}$ was detected, and the peak position is about −0.25 V (curve b). After capturing the dsDNA bond on the electrode surface through an amide, the peak of Fc was detected at about 0.3 V (curve c). When the fully constructed electrochemical sensor was immersed in a certain concentration of CEA for incubation, CEA was specifically recognized with its aptamer chain (S2-Fc), and Fc departed from the surface and the signal decreased. However, the signal of $[Ru(NH_3)_6]^{3+}$ remained almost unchanged (curve d). The results confirmed the feasibility of the constructed ratiometric biosensor for CEA detection based on the internal standard molecules.

After gradually modifying different materials on the electrode surface, the electrochemical behavior was shown in Fig. 3B. A redox peak of $[Ru(NH_3)_6]^{3+}$ was observed on bare MGE (curve a) , and the redox peak current increases obviously after the modification of MXC and further synthesis of Fe_3O_4 in situ (curve b and c), due to the perfect conductivity of the MXC, and a large increase of the specific surface area of the modified electrode.

3.6. Optimization of the proposed biosensor

In order to obtain the best sensing performance, various parameters, including the dosage of Fe^{2+} ($2Fe^{3+}$) in the synthesis of MXC-Fe_3O_4, the concentration of DNA, and the incubation time of CEA were optimized (Fig. S5). From Fig. S5A we can see that the zeta potential of MXC is about −35 mV before the addition of Fe^{2+} ($2Fe^{3+}$), the potential of MXC-Fe_3O_4 increased gradually when the concentration of Fe^{2+} ($2Fe^{3+}$) increased, and the concentration of Fe^{2+}($2Fe^{3+}$) reaches 8 mM, the zeta potential of MXC-Fe_3O_4 is about 0, meaning the closing to electric neutral of the material. Then the concentration of Fe^{2+} ($2Fe^{3+}$) was selected as the optimal concentration. As shown in Fig. S5B, with the increase of DNA concentration, the signal of Fc increase gradually and tends to be stable when DNA concentration reached 50 μM due to the saturated binding between the DNA and MXC-Fe_3O_4-Ru. Therefore, 50 μM is selected as the optimal concentration of S2-Fc. Fig. S5C shows the optimization of CEA incubation time, the DPV signal decreases with the increases of the CEA incubation time from 0 to 60 min, and the DPV signal nearly unchanged from 60 to 80 min, and the final choice was to incubate for 60 min for the detection.

3.7. Electrochemical detection of CEA

Under the optimized conditions, the biosensor was used to detect different concentrations of CEA. As shown in Fig. 4A, with the concentration of CEA increased, the DPV signal decreased gradually because the binding of CEA to Fc labeled aptamer and released from the electrode surface to the solution whereas DPV signal of the $[Ru(NH_3)_6]^{3+}$, as an internal standard signal, is basically constant. It can be observed that the corresponding regression equation in the detection range from 1 pg/mL to 1 μg/mL is $I_{Fc}/I_{Ru} = 2.905–0.215\log c$ (Fig. 4B) with a correlation coefficient of 0.9953. The corresponding detection limit is calculated to be 0.43 pg/mL by using 3σ/k. A series of measurements of AFP were used for estimating the precision, and the relative standard deviation (RSD) was less than 5.40%. As contrast, the electrochemical response of the biosensor to different concentrations of CEA without internal standard molecules was also studied as shown in Fig. 4C and D. The corresponding regression equation is $I_{Fc}/I_{Ru} = 2.905–0.215\log c$ (Fig. 4D) with a correlation coefficient of 0.9794. The results show that the detection accuracy is significantly improved by the internal standard method.

3.8. Stability, selectivity, and reproducibility of the biosensor

Fig. 5A shows that the DPV signal is changed slightly after DPV scans 50 times and after the electrode is treated in PBS solution for 48 h, the signal decreases by less than 7.00% (Fig. 5B). In addition, the signal of Fc has a significant downward trend in the process of stability test when the internal standard is not used (Fig. S6A and B, black curves). However, the internal standard method can effectively avoid this situation as can

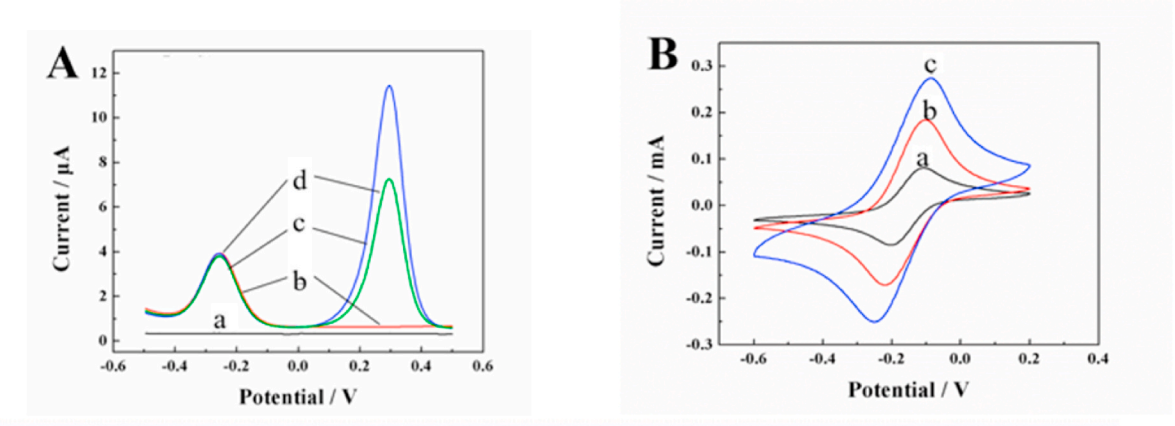

Fig. 3. (A) The construction process and feasibility of biosensor (a: bare MGE, b: MXC-Fe_3O_4-Ru/MGE, c: dsDNA/MXC-Fe_3O_4-Ru/MGE, d: after incubation in CEA); (B) CV curves of bare MGE (a), MXC/MGE (b) and MXC-Fe_3O_4/MGE(c) in 5 mM $[Ru(NH_3)_6]^{3+}$ at a scanning rate of 0.1 V/s.

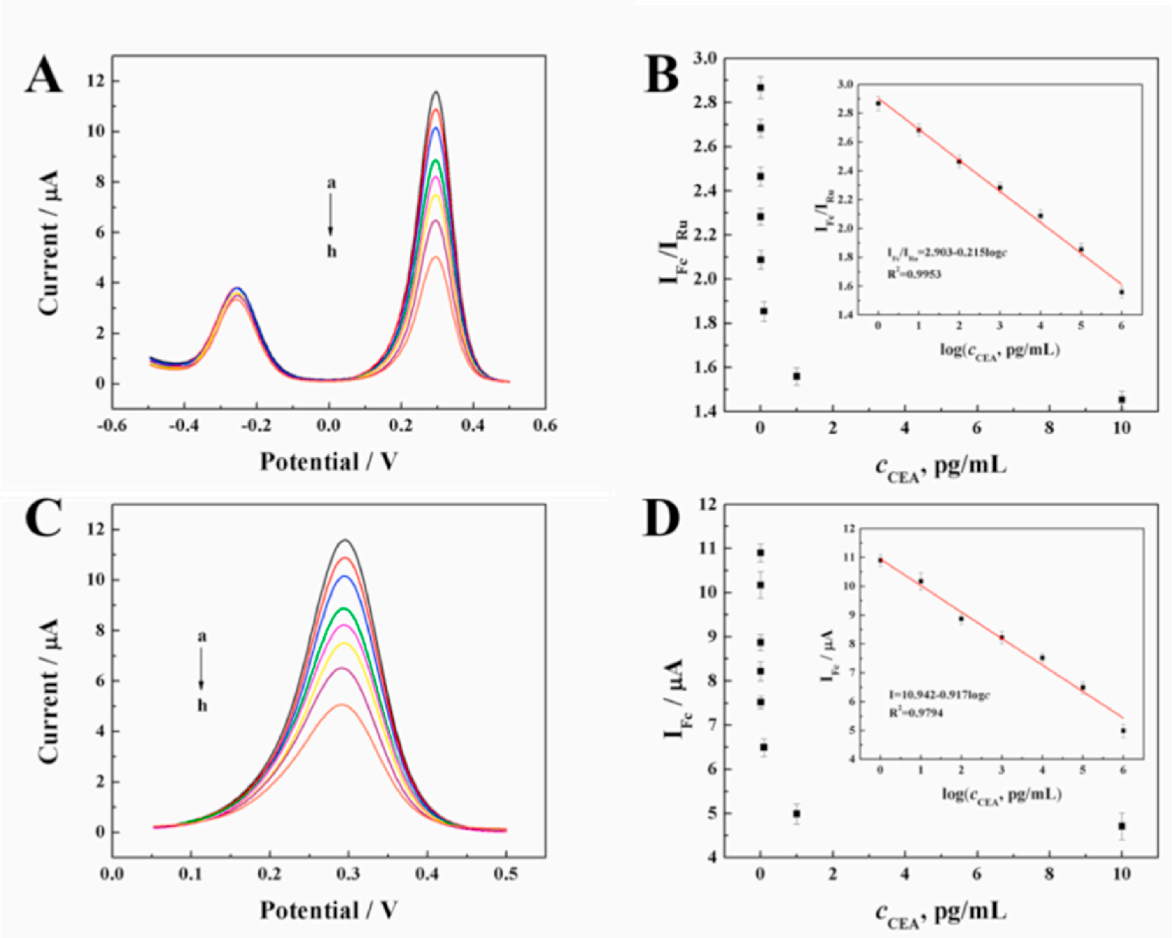

Fig. 4. (A) DPV responses of sensing interface to different concentrations of CEA: (a) 0 pg/mL, (b) 1 pg/mL, (c) 10 pg/mL, (d) 100 pg/mL, (e) 1 ng/mL, (f) 10 ng/mL, (g) 100 ng/mL (h) 1 μg/mL; (B) Logarithmic calibration curve of CEA concentration ($R^2 = 0.9953$); (C) Without internal standard, DPV responses of sensing interface to different concentrations of CEA; (D) Without internal standard, logarithmic calibration curve of CEA concentration ($R^2 = 0.9794$).

be seen in Fig. S6A (blue curve) and Fig. S6B (red curve). I_{Fc}/I_{Ru} in Fig. S6A and B are all almost unchanged, further proving the stability of the present biosensor.

Furthermore, the DPV responses of the electrochemical biosensor were incubated with four interferents [thrombin (TB), alpha fetoprotein (AFP), prostate specific antigen (PSA), and immunoglobulin G (IgG)] were investigated to evaluate the selectivity of CEA. As shown in Fig. 5C, Δ(IFc/IRu) increases significantly only in the presence of CEA, where (Δ(IFc/IRu) is the difference of IFc/IRu before and after reaction, showing the high selectivity of the biosensor. The reproducibility between five independent biosensors was also studied (Fig. 5D), and the relative standard deviation (RSD) between batches is 5.63%, indicating excellent reproducibility of the biosensor.

3.9. Clinical serum sample analysis

To prove the potential application of the electrochemical sensor, CEA clinical serum samples were measured and compared with the test results provided by the hospital using the standard ECL method. It can be seen from Table 1 that the CEA concentrations determined by the two methods were consistent with the RSD lower than 5.327%, And compared with various electrochemical sensors previously reported has better performance (Table 2). proving the reliability of the test results of the as-constructed electrochemical biosensor.

4. Conclusions

In summary, a ratiometric electrochemical biosensor based on new antifouling material was constructed. A novel antifouling material MXC-Fe_3O_4-Ru with excellent conductivity and internal standard molecule based on functional 2D nanomaterial MXC was synthesized for the first time which is a suitable choice for ratiometric detection strategy. The strong magnetism of MXC-Fe_3O_4-Ru is easy to separate and can be easily absorbed to the surface of the MGE, simplifying the modification process of the electrode, and there is no need to modify any other nonconducting antifouling materials due to its excellent antifouling performance, which ensures the electron transfer on the electrode surface. Excellent conductivity, antifouling performance, and ratiometric strategy make the sensor show remarkable sensitivity, selectivity, and accuracy, even in clinical serum samples. Thus, the electrochemical biosensor has the potential to be applied in clinical diagnosis and achieve satisfactory results.

CRediT authorship contribution statement

Huiqing Yang: Data curation, Formal analysis, Investigation, Methodology. **Yan Xu:** Data curation, Formal analysis, Investigation, Methodology. **Qianqian Hou:** Investigation, Validation, Supervision. **Qingzhang Xu:** Conceptualization, Supervision, Validation, Visualization, Writing – original draft. **Caifeng Ding:** Conceptualization, Writing – review & editing.

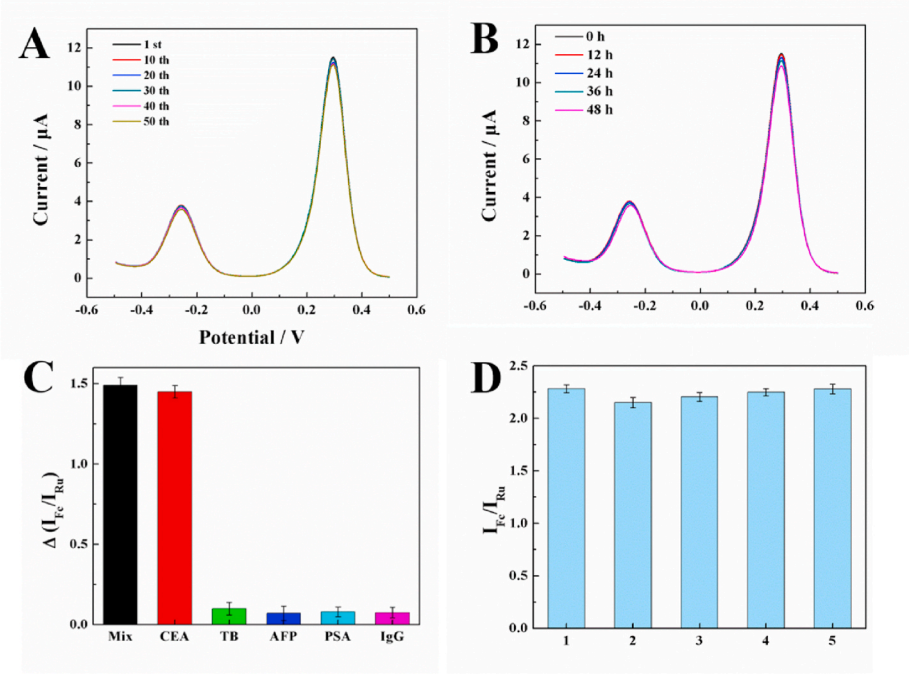

Fig. 5. (A) DPV response of the biosensor after 50 consecutive scans in PBS; (B) DPV response of the biosensor after being immersed in PBS for 48 h; (C) The selectivity of the biosensor to CEA; (D) The reproducibility of the biosensor.

Table 1
Analytical results of CEA in clinical serum samples[a] (n = 3).

Sample number	response time of this method (minute)	ECL method (ng/mL)	this method (ng/mL)	RSD (%)
1	60	1.762	1.720	−2.384
2	60	19.358	18.633	−3.745
3	60	25.207	26.561	5.372

[a] CEA clinical serum samples provided by the Affiliated Hospital of Heze Medical College.

Table 2
Comparison of different methods for CEA detection.

Analytical methods	Linear range/ng mL^{-1}	Limit of detection	References
Electrochemical immunosensor	0.1–1000	0.06 ng/mL	(Li et al., 2017)
Electrochemical aptasensor	0.01–100	0.84 pg/mL	Niu et al. (2022)
Electrochemical immunosensor	0.001–80	0.2 pg/mL	(Li et al., 2020)
Electrochemical biosensor	0.1–1000	0.33 ng/mL	(Song et al., 2021)
Electrochemical biosensor	0.001–1000	0.43 pg/mL	This work

Declaration of competing interest

The authors declare that they have no known competing financial interests or personal relationships that could have appeared to influence the work reported in this paper.

Acknowledgments

The authors greatly acknowledge support of the National Natural Science Foundation of China (22074074), and the Natural Science Foundation of Shandong Province (ZR2020MB065).

Appendix A. Supplementary data

Supplementary data to this article can be found online at https://doi.org/10.1016/j.bios.2022.114216.

References

Alhabeb, M., Maleski, K., Anasori, B., Lelyukh, P., Clark, L., Sin, S., Gogotsi, Y., 2017. Chem. Mater. 29, 7633–7644.
Breaker, R.R., 2004. Nature 432, 838–845.
Chimene, D., Alge, D.L., Gaharwar, A.K., 2015. Adv. Mater. 27, 7261–7284.
Cui, M., Song, Z.L., Wu, Y.M., Guo, B., Fan, X.J., Luo, X.L., 2016. Biosens. Bioelectron. 79, 736–741.
Ding, C.F., Wang, X.Y., Luo, X.L., 2019. Anal. Chem. 91, 15846–15852.
Ding, L., Wei, Y.Y., Li, L.B., Zhang, T., Wang, H.H., Xue, J., Ding, L.-X., Wang, S.Q., Caro, J., Gogotsi, Y., 2018. Nat. Commun. 9, 155.
He, Y., Li, J.H., Liu, Y., 2015. Anal. Chem. 87, 9777–9785.
Huang, K.J., Niu, D.J., Xie, W.Z., Wang, W., 2010. Anal. Chim. Acta 659, 102–108.
Hui, N., Sun, X.T., Niu, S.Y., Luo, X.L., 2017. ACS Appl. Mater. Interfaces 9, 2914–2923.
Kim, S.H., Lee, J., Lee, B.H., Song, C.-S., Gu, M.B., 2019a. Biosens. Bioelectron. 134, 123–129.
Kim, S.H., Nam, O., Jin, E., Gu, M.B., 2019b. Biosens. Bioelectron. 123, 160–166.
Li, K.K., Jiao, T.F., Xing, R.R., Zou, G.D., Zhao, Q.R., Zhou, J.X., Zhang, L.X., Peng, Q.M., 2018a. Green Energy Environ. 3, 147–155.
Li, K.K., Zou, G.D., Jiao, T.F., Xing, R.R., Zhang, L.X., Zhou, J.X., Zhang, Q.R., Peng, Q. M., 2018b. Colloids Surf. A Physicochem. Eng. Asp. 553, 105–113.
Li, W.J., Ma, C.Y., Song, Y.J., Hong, C.L., Qiao, X.W., Yin, B.C., 2020. Nanotechnology 31, 185605.
Li, Y., Chen, Y., Deng, D.M., Luo, L.Q., He, H.B., Wang, Z.X., 2017. Sensor. Actuator. B 248, 966–972.
Liang, X., Garsuch, A., Nazar, L.F., 2015. Angew. Chem. Int. Ed. 127, 3979–3983.
Liu, N.Z., Hui, Ni, Davis, J.J., Luo, X.L., 2018. ACS Sens 3, 1210–1216.
Liu, J., Jiang, X.T., Zhang, R.Y., Zhang, Y., Wu, L.M., Lu, W., Li, J.Q., Li, Y.C., Zhang, H., 2018. Adv. Funct. Mater. 29, 1807326.
Liu, B.S., Liu, X., Shi, S., Huang, R.L., Su, R.X., Qi, W., He, Z.M., 2016. Acta Biomater 40, 100–118.
Lu, Y.B., Lu, X.Y., Gu, S.T., Shi, X.-M., Fan, G.-C., 2021. Sensor. Actuator. B 343, 130060.
Luo, X.L., Xu, Q., James, T., Davis, J.J., 2014. Anal. Chem. 86, 5553–5558.
Ma, L.Z., Zhang, D.Q., Zhao, P.W., Wang, B., Luo, X.L., 2021. Sensor. Actuator. B 345, 130365.
Martín, M., Salazar, P., Álvarez, R., Palmero, A., López-Santos, C., González-Mora, J.L., González-Elipe, A.R., 2017. Sensor. Actuator. B Chem. 240, 37–45.
Miao, J.J., Wang, X.B., Lu, L.D., Zhu, P.Y., Mao, C., Zhao, H.L., Song, Y.C., Shen, J., 2014. Biosens. Bioelectron. 58, 9–16.
Naguib, M., Mochalin, V.N., Barsoum, M.W., Gogotsi, Y., 2014. Adv. Mater. 26, 992–1005.

Niu, C., Lin, X.J., Jiang, X., Guo, F., Liu, J.X., Liu, X.Q., Huang, H.G., Huang, Y., 2022. Bioelectrochemistry 143, 107986.
Qiu, Z.L., Shu, J., Tang, D.P., 2018. Anal. Chem. 90, 1021–1028.
Raston, N.H.A., Gu, M.B., 2015. Biosens. Bioelectron. 70, 261–267.
Smith, C.L., 2013. US Pat. Appl, 13621525.
Song, J.Y., Teng, H., Xu, Z.Y., Liu, N.Z., Xu, L., Liu, L., Gao, F.X., Luo, X.L., 2021. Mikrochim. Acta 188, 217.
Song, Y.L., Zhu, Z., An, Y., Zhang, W.T., Zhang, H.M., Liu, D., Yu, C.D., Duan, W., Yang, C.Y.J., 2013. Anal. Chem. 85, 4141–4149.
Steward, A.M., Nixon, D., Zamcheck, N., Aisenberg, A., 1974. Cancer 33, 1246–1252.
Sun, F., Hung, H.-C., Sinclair, A., Zhang, P., Bai, T., Galvan, D.D., Jain, P., Li, B.W., Jiang, S.Y., Yu, Q.M., 2016. Nat. Commun. 7, 13437.
Tang, Juan, Tang, D.P., Niessner, R., Chen, G.N., Knopp, D., 2011. Anal. Chem. 83, 5407–5414.
Wang, G.X., Han, R., Li, Q., Han, Y.F., Luo, X.L., 2020. Anal. Chem. 92, 7186–7193.
Wang, G.X., Xu, Q.J., Liu, L., Su, X.L., Lin, J.H., Xu, G.Y., Luo, X.L., 2017. ACS Appl. Mater. Interfaces 9, 31153–31160.
Wu, Z.J., Li, H., Liu, Z.H., 2015. Sensor. Actuator. B 206, 531–537.
Xu, Y., Wang, X.Y., Ding, C.F., Luo, X.L., 2021. ACS Appl. Mater. Interfaces 13, 20388–20396.
Yadav, N., Singh, A., Kaushik, M., 2020. J. Mater. Sci. Mater. Med. 31, 68.
Yan, J., Ren, C.E., Maleski, K., Hatter, C.B., Anasori, B., Urbankowski, P., Sarycheva, A., Gogotsi, Y., 2017. Adv. Funct. Mater. 27, 1701264.
Zhang, H.X., Wang, Z.H., Wang, F., Zhang, Y.M., Wang, H.Y., Liu, Y., 2021. Talanta 224, 121879.
Zhang, H.X., Wang, Z.H., Wang, F., Zhang, Y.M., Wang, H.Y., Liu, Y., 2020. Anal. Chem. 92, 5546–5553.
Zhang, X.N., Brodus, D.S., Hollimon, V., Hu, H.M., 2017. Chem. Cent. J. 11, 18.
Zhou, S.W., Wang, Y.Y., Zhu, J.-J., 2016. ACS Appl. Mater. Interfaces 8, 7674–7682.
Zhuang, X.D., Mai, Y.Y., Wu, D.Q., Zhang, F., Feng, X.L., 2015. Adv. Mater. 27, 403–427.